Eng Int Syst (2023) 1: 33–42

Engineering
Intelligent Systems

Longitudinal Deformation Analysis of High-Resolution Integrated Images Based on Multi-Sensors

Hongjie Chen[1,*] **and Chuan Xiao**[2]

[1] *Information Engineering Department, Yantai Gold College, Zhaoyuan 265401, China*
[2] *College of Engineering, Yantai Nanshan University, Yantai 265713, China*

In order to improve the quality of high-resolution integrated images, a longitudinal deformation analysis method is applied to such images based on multi-sensors. The high-resolution integrated images are collected by CMOS (complementary metal oxide semiconductor) and CCD (charge-coupled device) image sensors, and are then fused using the Laplace shape decomposition method. The fast ICA algorithm is applied to enhance the fused high-resolution integrated images. Based on the processed images, a high-resolution integrated image longitudinal deformation model is constructed, and the model is trained by an implicit support vector machine. The longitudinal deformation analysis results of the high-resolution integrated image are obtained by combining the longitudinal deformation distances. According to experimental results, the proposed method has high analytical accuracy, good image longitudinal deformation processing, high level of efficiency in terms of longitudinal deformation analysis, and good practical application.

Keywords: Multi-Sensor; High-Resolution Integrated Image; Longitudinal Deformation; Laplace Shape Decomposition Method; Fast ICA Algorithm; Deformation Distance

1. INTRODUCTION

Over the past few decades, CCD image sensors have dominated the image sensor market [1,2]. However, these sensors have several disadvantages: it is difficult to integrate monolithically the driving circuit and the signal processing circuit with the imaging array, high voltage is required, the yield is low, and the cost is high [3]. The CMOS image sensor is not a recent development. It emerged almost at the same time as the research on the charge-coupled device (CCD) image sensor. However, the technology at that time was not advanced; hence, the images captured by CMOS sensors were poor quality, and had low resolution and noise reduction, and the light sensitivity is not enough, so CMOS sensors have largely been ignored and not improved. In order to overcome these shortcomings, the development of CMOS image sensors has been carried out abroad [4]. With the continuous development of standard CMOS large-scale integrated circuit technology, the technical difficulties associated with the manufacture of the earlier CMOS image sensor have found corresponding solutions, thus greatly improving CMOS image sensors [5]. The CMOS image sensor itself has the incomparable advantages of CCD devices, such as the monolithic integration of pixel array and processing circuit, low voltage, low system complexity and low cost. Therefore, a high-quality, low-cost CMOS image sensor has been designed and manufactured [6]. CMOS and CCD image sensors have attracted worldwide attention since their appearance, and their applications involve various industries such as agriculture, forestry, land, surveying and mapping, transportation, water conservancy, electric power, military, environmental monitoring and management. Combining the advantages of these two sensors, high-resolution integration using multi-sensor acquisition has become possible. A target

*Email of corresponding author: ythjchj2022@126.com

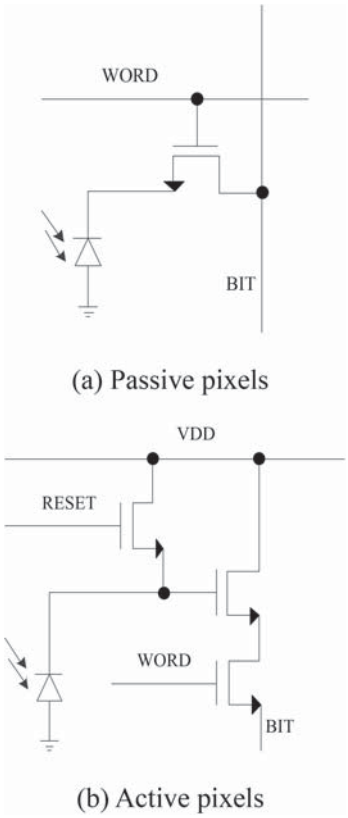

Figure 1 CMOS image sensor pixel structure.

to be detected in a high-resolution integrated image will change due to various factors, which makes image target detection very difficult. Among the factors contributing to this change are not only the changes in illumination and angle, but also changes in scale deformation, intra-class shape, and other visual properties. Of these, longitudinal deformation will lead to a significant decrease in image quality and affect the accuracy of target detection. Therefore, the study of a method for longitudinal deformation analysis of high-resolution integrated images is of great significance. Hence, this paper proposes a multi-sensor-based, high-resolution integrated image longitudinal deformation analysis method. The proposed method and its feasibility and validity are verified by experiments.

2. DESIGN OF LONGITUDINAL DEFORMATION ANALYSIS METHOD FOR HIGH-RESOLUTION INTEGRATED IMAGES

2.1 High-Resolution Integrated Image Acquisition

2.1.1 High-Resolution Integrated Image Acquisition Based on Multiple Sensors

(1) CMOS image sensor

A CMOS image sensor comprises photosensitive devices, amplifier circuits, A/D conversion circuits, timing generation circuits, digital signal processing circuits, etc. on a single chip by means of an integrated circuit processing technology. It has a high degree of integration and powerful functions. It is characterized by good stability and low cost, and extensive application prospects [7,8]. The CMOS image sensor is mainly composed of a pixel photosensitive unit array and auxiliary circuits. The pixel photosensitive unit array is the core component. It mainly converts the received optical signal into an electrical signal to realize the function of photoelectric transformation, thereby facilitating image acquisition. The different pixel structures of CMOS image sensing can be divided into two types: passive and active. The pixel structure is shown in Figure 1.

The auxiliary circuit inside the sensor is the key element responsible for collection and transmission, and functions such as timing drive, signal amplification, A/D conversion and interface output [9]. The configuration of a typical image sensor is shown in Figure 2.

The photo sensitive pixel units are arranged in a two-dimensional array along both X direction and Y direction respectively. Each pixel unit has its own unique coordinate address in both X direction and Y direction in the array. And the pixel output can be determined by the X and Y directions and controlled by the address decoder. In each column of pixels, there is a corresponding column amplifier, and the output signal of the column amplifier is connected with the multi-channel analog switch (MCAS), and the address decoder in the direction controls the MCAS [10,11]. When the image sensor works normally, the corresponding analog switch on the row pixel unit is controlled by the address decoder in the Y direction. When the switch is turned on, the

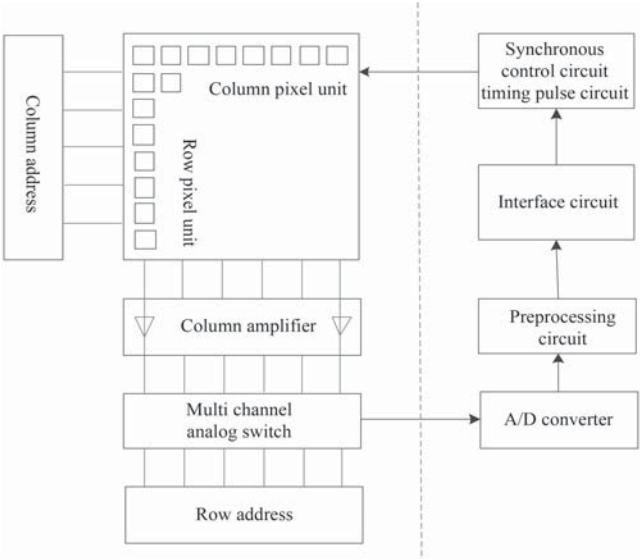

Figure 2 Organizational structure of CMOS image sensor.

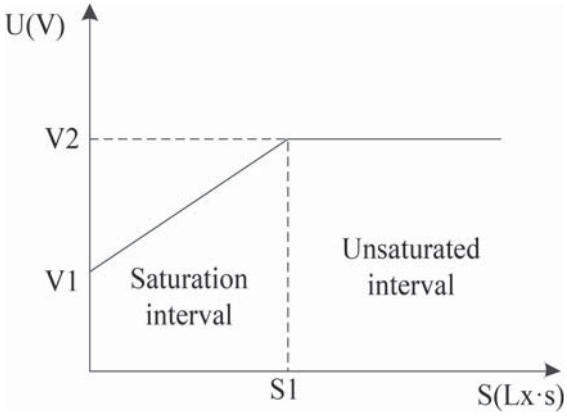

Figure 3 Photoelectric transformation characteristics of CCD devices.

signal of the pixel is transmitted to the corresponding column through the row analog switch, and the address is passed through the X direction. The control signal of the decoder is transmitted to the amplification module, and the A/D conversion module performs A/D conversion on the received output signal of the amplification module and transmits it to the signal preprocessing module. This is output to the outside through the sensor module for external circuit calling.

(2) CCD image sensor

CCD is a semiconductor device consisting of many neatly-arranged photodiodes which can sense light and transform the light signal into an electrical signal, which is then transformed into the digital image signal by an external sampling amplifying circuit and an analog-to-digital (A/D) conversion circuit. Being a photoelectric transformation device as well, CCD contains a photosensitive unit, and an input structure and output structure. Its basic function is to generate, store, transmit and detect a signal charge. Its prominent feature is that the charge serves as signal [12]. The photoelectric transformation characteristics of the CCD device are shown in Figure 3.

On the coordinate axis, the abscissa S represents the amount of exposure, and the ordinate represents the output voltage. It can be seen that when the light integration time set by the CCD device is too lengthy, or the received light intensity is too great, the charge in the CMOS potential trap will become saturated and may even overflow, interfering with the signal of the adjacent photosensitive unit. The increase of the CCD output signal reduces the sharpness of the image, and even causing the image to be blurred and seriously distorted. Usually, in order to reduce the luminous flux obtained at the CCD pixel point, the light integration time is decreased, the aperture is narrowed or a neutral attenuation filter is placed in front of the optical lens. The upper limit of the CCD temperature measurement range depends on the CCD saturation output voltage size and the camera exposure time, that is, the integration time of the CCD device.

The color CCD camera embeds red (R), green (G), and blue (B) color filters on the surface of the CCD sensor to separate colors and capture images. The three primary colors specified by the International Commission on Illumination are: red $\lambda_r = 700nm$, green $\lambda_g = 546.1nm$, and blue $\lambda_b = 435.8nm$. According to the principle of three primary colors, any color can be created by using these three primary colors. The spectral response characteristic curve of the three primary color signals of the color CCD camera is shown in Figure 4.

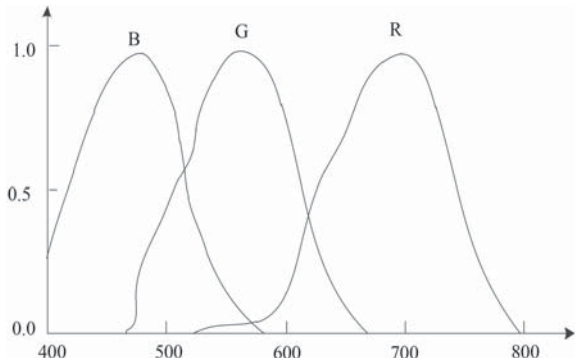

Figure 4 CCD spectral response characteristic curve.

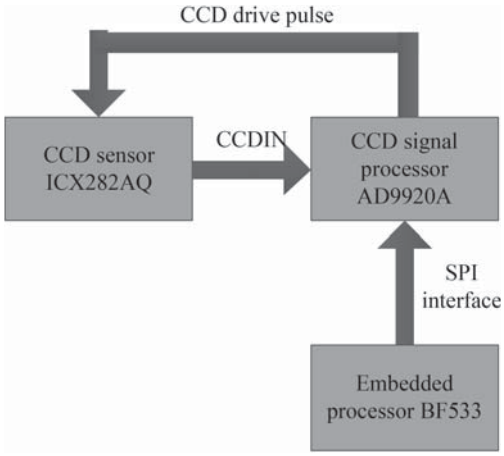

Figure 5 CCD image acquisition module.

The abscissa in the figure represents the light wavelength (unit is nm), and the ordinate represents the relative value of the output signal response of the CCD (dimensionless, the maximum value is 1).

It can be seen from Figure 4 that the spectral response bands of the color components R, G, and B of the CCD photosensitive unit are diff erent, as is the radiant energy of each component. The channel output values of the three primary colors of the color CCD have a linear relationship with the monochromatic radiance of the high-temperature radiator within a certain range. If the CCD works in the linear region, the ideal monochromatic response can be assumed for the spectral response characteristics of the CCD. The color CCD camera's spectral response range is within the visible light band (380nm–780nm). If the spectral response characteristic functions of the three primary color signals of the color CCD are $r(\lambda)$, $g(\lambda)$ and $b(\lambda)$, then the R, G, B of each pixel of the color CCD camera is:

$$\begin{cases} R = A\int_{380}^{780} L(\lambda, T)r(\lambda)dr \\ G = A\int_{380}^{780} L(\lambda, T)g(\lambda)dr \\ B = A\int_{380}^{780} L(\lambda, T)b(\lambda)dr \end{cases} \quad (1)$$

The CCD image acquisition module is shown in Figure 5.

The internal registers of the CCD signal processor can be accessed through the SPI interface, and the registers of the CCD signal processor AD9920A are written through the SPI interface of the embedded processor BF533 to generate the CCD drive pulse signal required by the ICX282AQ sensor: vertical drive pulse signal, horizontal drive pulse signal, shutter control signal. The output pixel signal of the CCD sensor ICX282AQ is stored in the FIFO buffer of USB2.0 after AD conversion.

2.1.2 Image Fusion Processing

The image tower decomposition-based, high-resolution integrated image fusion method is used for multi-resolution and multi-scale image fusion. The fusion process is carried out at various scales, spatial resolutions and decomposition layers. This fusion is based on Laplace shape decomposition and consists of two parts:

(1) Laplace-shaped decomposition of the image

The steps used to create a Laplace-shaped decomposition of an image are explained below. Assuming the original image is G_0, the bottom layer of the Gaussian pyramid is G_0 [13], and the l-th layer image G_l is constructed as follows: first convolve the $l-1$-layer image G_{l-1} with a window function $w(m, n)$ having low-pass characteristics, and then convolve the result. For down-sampling of every row and every column, that is:

$$G_l = \sum_{m=-2}^{2}\sum_{n=-2}^{2} w(m, n)G_{l-1}(2i + m, 2j + n) \quad (2)$$

Among them, $0 \le l \le N.N$ is the top layer number of the Gaussian pyramid. C_l refers to columns of the l-th layer image, and R_l refers to rows of the l-th layer image; $w(m, n)$ should satisfy the separable condition, namely:

$$w(m,n) = w(m)w(n) \tag{3}$$

Among them, $w(0) = a,\ w(1) = w(-1) = 0.5,\ w(2) = w(-2) = \frac{a}{2},\ a$ takes the value 0.4. The reduction operator Reduce is introduced to simplify writing; then Formula (2) is written as:

$$G_l = \mathrm{Re}duce(G_{l-1}) \tag{4}$$

In this way, the Gaussian pyramid is comprised of $G_0, G_1, \ldots, G_N$. where G_0 is the pyramid's bottom layer and G_N is the pyramid's top layer. The total number of Gaussian pyramid layers is $N + 1$ [14]. The Gaussian pyramidal decomposition of the visible image is obtained by sequentially convolving the low-level image with the weight function $w(m, n)$ having low-pass characteristics, and then down-sampling the convolution result with each row and each column. Since the image size of each layer decreases from the bottom layer to the top layer of the pyramid, and the size of the upper layer image is equal to 1/4 of the image size of the previous layer, it can be considered that the Gaussian pyramid is a multi-resolution, multi-scale, low-pass filter. [15].

G_l is interpolated to enlarge, resulting in an enlarged image G_l^*. In this way, G_l^* and G_{l-1} are the same size. The mathematical formula is:

$$G_l^* = 4 \sum_{m=-2}^{2} \sum_{n=-2}^{2} w(m,n) G_l^{'} \left(\frac{i+m}{2}, \frac{j+n}{2} \right) \tag{5}$$

In order to simplify writing, the enlargement operator Expand is introduced, namely:

$$G_l^* = Expaand(G_l) \tag{6}$$

G_l^* is the same size as G_{l-1}, but G_l^* is not equal to G_{l-1}. It can be seen from Formula (6) that the gray value of the new pixel interpolated between the original pixels is determined by the weighted average of the gray value of the original pixel [16]. Because G_l is obtained by low-pass filtering G_{l-1}, G_l^* contains less detailed information than G_{l-1}. Make:

$$\begin{cases} LP_l = G_l - Expand\ (G_{l+1}), 0 \le 1 < N \\ LP_N = G_N, 1 = N \end{cases} \tag{7}$$

In the formula, LP_l is Laplace shape decomposition's l-th layer image.

In this way, the Laplacian pyramid consists comprised of $LP_0, LP_1, \ldots, LP_N$. Each layer of the image refers to the difference between the Gaussian pyramid image and the upper layer image after being enlarged by the magnification operator, which is equivalent to bandpass filtering. Therefore, the Laplacian pyramid is also known as 'bandpass tower decomposition'.

According to Formula (7), we can get:

$$\begin{cases} G_l = LP_l + Expand\ (G_{l+1}), 0 \le 1 < N \\ G_{NN} = LP, 1 = N \end{cases} \tag{8}$$

Starting from the Laplacian pyramid's top layer and going from top to bottom, recursively according to Formula (8), the relevant Gaussian pyramid can be restored, and the original image G_0 can finally be acquired. After derivation, Formula (8) can be expressed as:

$$G_0 = \sum_{l=0}^{N} LP_{l,l} \tag{9}$$

Formula (9) shows that the image of each layer of the Laplacian pyramid is gradually interpolated and enlarged by the Expand operator until it is the same size as the original image, and then added together to reconstruct the original image G_0.

(2) Image fusion method based on Laplace shape decomposition

The image fusion process depending on a certain tower-shaped decomposition is performed independently on the images of each decomposition layer. The basic steps of high-resolution integrated image fusion on the basis of Laplace shape decomposition are described below.

Decompose two images that will be fused by Laplacian shape respectively, and establish the Laplacian pyramid for each image.

Separately fuse each decomposition layer of the image pyramid. Various decomposition layers can adopt various fusion rules. Finally, the Laplacian pyramid of the fused image is obtained.

The image reconstruction is performed on the Laplacian pyramid of the fused image, and the obtained reconstructed image is the fused image.

2.2 Image Enhancement Processing

As a new blind source separation (BSS) technology which has been developed in recent years for independent component analysis (ICA) is a new method of signal processing and data analysis based on signal high-order statistics [17]. ICA has three basic models: general model, noise model and noise-free model. In practical applications, the noise is usually ignored. The noise-free ICA model is used to enhance the fused high-resolution integrated image.

$$x = A \cdot s \tag{10}$$

where $s = [s_1, s_2, \ldots, s_N]^T$ is the source signal. A refers to a $M \times N$ dimensional matrix, and $x = [x_1, x_2, \ldots, x_N]^T$ refers to the observation signal. The usual additional assumptions are:

(1) $m \ge n$;

(2) Source signals s_i are statistically independent of each other;

(3) At most one source signal is Gaussian;

(4) A is the full rank matrix;

(5) Each source signal has zero mean and unit power.

The target of ICA is to predict the separation matrix W and separate the source signal s from the observation signal x, that is:

$$y = W \cdot x \tag{11}$$

If y_i is as independent as possible, then y_i is approximately regarded as s_i.

The point of ICA algorithm is to judge y_i, the statistical independence degree. This paper uses the method of nonlinear uncorrelation to measure independence.

For statistically independent source signal vectors, the joint probability density is separable, and the arbitrary order joint moments of independent random variables are also separable. Assuming that there are two independent sources S_1 and S_2, there are:

$$p(S_1, S_2) = p(S_1)p(S_2) \tag{12}$$

$$E\{S_1^{k_1} S_2^{k_2}\} = E\{S_1^{k_1}\}E\{S_2^{k_2}\} \tag{13}$$

where k_1 and k_2 are integers greater than zero. The general description is:

$$E\{f(S_1)g(S_2)\} = E\{f(S_1)\}E\{g(S_2)\} \tag{14}$$

where f and g refer to two nonlinear functions. The Formula 14 above shows that the nonlinear uncorrelation of random variables means that they are independent of each other. Therefore, the independence of ICA output results can be achieved by introducing nonlinear link $g(\cdot)$ at the output of ICA model. The independence of the separation results is measured by calculating the covariance matrix of the nonlinear output. Obviously, if the components of the output vector $y = (y_1, y_2, \ldots, y_N)^T$ are independent of each other. Not only its covariance matrix C_y but also the covariance matrix C_Z of its nonlinear output $z = (z_1, z_2, \ldots, z_N)^T$ are a diagonal matrix.

The FastICA algorithm, also known as a fixed-point algorithm, is a quick optimization iterative algorithm. The diff erence between general algorithms and ordinary neural network algorithm lies in that this algorithm adopts batch processing. In other words, a large number of sample data participate in the operation in each iteration. However, seen from distributed parallel processing, this algorithm can still be regarded as a neural network algorithm. Fast ICA algorithm is based on kurtosis, maximum likelihood and negative entropy. This paper highlights the FastICA algorithm based on negative entropy. Compared with other ICA algorithms, the FastICA algorithm has many advantages: for example, it has fast convergence speed, requires no selection of step parameters. It is easy to use, and can be optimized by selecting appropriate nonlinear function $g(\cdot)$, parallel, distributed, simple calculation, few memory requirements, etc.

The FastICA algorithm consists of two parts: observation signal preprocessing and independent component extraction. Signal preprocessing includes centralization and whitening. Centralization involves subtracting the average value to make x a variable with a median of 0, which simplifies the calculation. Whitening is the linear transformation of observation signal x into v with unit variance and uncorrelated components through PCA network. Since whitening can eliminate the correlation among observation signals, it also simplifies the extraction of subsequent independent components.

Next, the whitening signal v is further processed; that is, the matrix W is found according to the negative entropy criterion in order to separate the independent components. By selecting W, $J(y)$ is the largest. According to Formula (14), $J(y)$ is the largest, that is, $E\{G(y)\}$ is the largest. Find the extreme value of $E\{G(y)\} = E\{G(w^T x)\}$, $E\{G(y)\} = E\{G(w^T x)\} = 0$, g is the derivative of $G(\cdot)$, and $g^{'}(\cdot)$ is the derivative of $g(\cdot)$. According to Newton's iterative theorem:

$$\begin{cases} w^+ = \frac{w - [E\{xg(w^T x)\} - \beta w]}{E\{g^{'}(w^T x)\} - \beta} \\ w* = \frac{w^+}{\|w^+\|} \end{cases} \tag{15}$$

where $\beta = E\{xg(w^T x)\}$, w^+ is the Newton iteration result, and w^* is the updated value after normalization of w^+. By simplify ing the above formula, the following fixed-point ICA algorithm can be obtained:

$$\begin{cases} w^+ = E\{xg(w^T x)\} - E\{g^{'}(w^T x)\}w \\ w^* = \frac{w^+}{\|w^+\|} \end{cases} \tag{16}$$

The method for removing the extracted independent component is as follows (assuming that k component has been estimated):

$$w_{k+1} = w_k - \sum_{j=1}^{k} w_{k+1}^T w_j \tag{17}$$

If it does not converge, repeat this process until it converges, and an independent component can be estimated. If there are n source signals, n independent components must be estimated. After extracting one component at a time, subtract the independent component from the observation signal and repeat until all components are extracted to complete the enhancement of the high-resolution integrated image.

2.3 Longitudinal Deformation Analysis of High-Resolution Integrated Image

(1) Build image longitudinal deformation model

It is assumed that $G = (V, E)$ represents the object model in the high-resolution integrated image. $V = \{v_1, v_2, \ldots, v_n\}$ represents n parts, and $(v_i, v_j) \in E$ represents the connection between the two parts. A certain position layout of an object can be expressed as $L = \{l_1, l_2, \ldots, l_n\}$, and 1_i represents the position of v_i. If $m_i(l_i)$ is used to measure the degree of mismatch with the template at position f_i in the high-resolution integrated image v_i, and $d_{iJ}(l_i, l_J.)$ is used to measure the degree of change of the model when v_i and v_j are at positions l_i and l_j in the image respectively. Then, when each block in the model matches the image best, and the layout with the closest relative relationship between the blocks and the model after block matching is the best position layout of an image relative to the model. The optimal location layout can be described by the following formula:

$$L^* = \arg_L \min \left(\sum_{i=1}^{n} m_i(l_i) + \sum_{(v_t, v_J) \in E} d_{iJ}(l_i, l_j) \right) \tag{18}$$

A deformation model with n blocks can be expressed as $(F_0, P_1, \ldots, P_n, b)$, where F_0 represents root filter, P_i represents the model of the i-th block in the model, and b represents an offset term. Each block in the deformation

model can be represented as (F_i, v_i, d_i), where F_i is the i-th block filter. v_i is a two-dimensional vector representing the "anchor" position of the i-th block filter relative to the root filter position, and d_i is a four-dimensional vector representing a deformation cost of the j-th block filter relative to its "anchor" position, which is measured by a quadratic function. Then the score of a deformation model consists of the following parts: the score of each filter's respective position, the deformation cost of each block filter corresponding to its "anchor" position and an offset term, which can be expressed by the following formula:

$$score(p_0, \ldots, p_n) = \sum_{i=0}^{n} F_i^{'} \cdot \emptyset(H, p_i) - \sum_{i=1}^{n} d_i \emptyset_d \times (dx_i, dy_i) + b \quad (19)$$

of which:

$$(dx_i, dy_i) = (x_i, y_i) - (2(x_0, y_0) + v_i) \quad (20)$$

represents an offset of the i-th block filter in the deformation model corresponding to its "anchor" position. Then there is:

$$\emptyset_d(dx, dy) = (dx, dy, dx^2, dy^2) \quad (21)$$

where $\emptyset_d(dx, dy)$ represents the deformation eigenvector, and the second term in Formula (21) represents the deformation cost.

If the state of the filter in an image area to be detected is called a hypothesis and expressed by $z = \{p_1, p_2, \ldots, p_n\}$, the score function can be represented in the form of $\beta \cdot \psi(H, z)$, where β is a vector of various parameters of the model. β and $\psi(H, z)$ are respectively expressed as follows:

$$\beta = (F_0^{'}, \ldots, F_n^{'}, d_1, \ldots, d_n, b) \quad (22)$$

$$\psi(H, z) = (\emptyset(H, p_0), \ldots, \emptyset(H, p_n), \emptyset_d(dx_1, dy_1), \ldots, \emptyset_d \times (h_n, dy_n), 1) \quad (23)$$

(2) Model training

The learning of the model involves the learning of the model parameters, which can be done with the relatively simple and practical SVM method. However, the position of the block filter relative to the root filter in the model is unknown, so the SVM method cannot meet the needs of model parameter learning. Therefore, the latent SVM method is proposed. A significant advantage of latent SVM is that it will eventually become a semi-convex problem like a conditional random field. If the latent information is defined as a positive example, the training problem becomes a convex problem. The training process is described in detail below.

An implicit support vector machine (ISVM) can use the following formula to represent the classifier that can express the score of sample x:

$$f_\beta(x) = \max_{z \in Z(x)} \beta \cdot \emptyset(x, z) \quad (24)$$

where z represents an implied value. $Z(x)$ is set to define all possible implied values of sample x. The determination of sample x can be realized by thresholding $f_\beta(x)$. Compared with the classical SVM algorithm, the marked sample set $D = (\{x_1, y_1\rangle, \ldots, \{x_n, y_n\rangle)$ is defined, and the parameter β is trained by objective function (24) minimization:

$$L_D(\beta) = \frac{1}{2}\|\beta\|^2 + C \sum_{i=1}^{n} \max(0, 1 - y_i f_\beta(x_i)) \quad (25)$$

where $\max(0, 1 - y_i f_\beta(x_i))$ represents standard "hinge loss", and constant C achieves the control of the relative weight of the regular term. Note that if there is only one implicit value, that is, $|Z(x_i)| = 1$, then f_β to β is linear. At this time, the linear support vector machine can be regarded as a special case of implicit support vector machine.

If Z_p represents a set of implied values of every positive sample in the training set D, an auxiliary objective function can be defined

$$L_D(\beta, Z_p) = L_{D(z_p)}(\beta) \quad (26)$$

where D_{Z_p} is derived from the training set D by limiting the implied value of each positive sample. That is, z_i in set $Z(x_i) = \{z_i\}$ represents an implied value of sample x_i. Then the goal becomes minimization $L_D(\beta, Z_p)$:

$$L_D(\beta) = \min_{Z_p} L_D(\beta, Z_p) \quad (27)$$

In practical application, the method of cooperative descent is used to minimize $L_D(\beta, Z_p)$.

The specific steps are:

(1) Re-label positive samples: optimize Z_p of $L_D(\beta, Z_p)$ by selecting the implied value of positive samples that can maximize $f(x)$.

(2) Optimization parameter β: optimize the parameters in $L_D(\beta, Z_p)$ by solving the convex programming problem of $L_{D(z_p)}(\beta)$.

Apply the two steps above, continuously improve the value of $L_D(\beta, Z_p)$ until convergence, when a local optimum will be obtained. The longitudinal deformation of high-resolution integrated image is analyzed by using the trained longitudinal deformation model of high-resolution integrated image, and the relevant analysis results are obtained. The specific formula is:

$$D = \frac{L_D(\beta, Z_p) \sum_{p=1}^{N} (u(p)^2 + v(p)^2)^{\frac{1}{2}}}{N_S} \quad (28)$$

where N is the total number of pixels of the original high-resolution integrated image, and N_S is the number of SIFI points matched between the original image and the actual image. The larger the value of D (i.e., the longitudinal deformation distance), the greater will be the distortion of the target image, while the smaller the value of D (i.e., the longitudinal deformation), the less will be the image distortion.

3. EXPERIMENTAL DESIGN

To determine the effectiveness of the proposed method, several experimental tests were conducted.

Figure 6 Images of some experimental samples.

To ensure the authenticity and reliability of experimental results, various parameters were established for the experiments: tests were conducted using a computer with 10 core Intel Xeon E5-2640 CPU, 64GB memory, HDD 10TB hard disk and Window 10 operating system, and the simulation software was MATLAB 7.2.

The sensor was used to collect the images of multiple experimental samples. After integration and screening, 2000 experimental samples were selected for testing, of which 500 sample data were used as training samples, and the other 1500 data were used as experimental samples. Several experimental samples are shown in Figure 6.

The longitudinal deformation of high-resolution integrated image is analyzed using this method, and the results are shown in Figure 7.

By analyzing the results shown in Figure 7, it can be seen that the position of longitudinal deformation in each image can be accurately found by using this method, thereby proving the high level of accuracy that can be achieved by the proposed method, and broadening its application.

These high-resolution integrated images with longitudinal deformation are further processed using this method to obtain higher quality image processing results, as shown in Figure 8.

By analyzing the longitudinal deformation processing results of the high-resolution integrated image in Figure 8, it can be seen that these problematic images can be restored according to the longitudinal deformation position recognition results of the high-resolution integrated image obtained by this method. The processed image does not have the problem of longitudinal deformation, and the image quality is better, which can effectively solve the problem of longitudinal deformation of the high-resolution integrated image.

Using the method proposed in this paper, 1500 experimental samples were divided into 10 groups on average, and the time required for the longitudinal deformation of high-resolution integrated images was calculated. Table 1 shows the experimental results.

The data in Table 1 shows that the maximum time taken to analyze the longitudinal deformation of high-resolution integrated image by this method is 2.56s, the minimum value is 1.35s, and the average value is 1.76s. Therefore, the time taken by this method to analyze the longitudinal

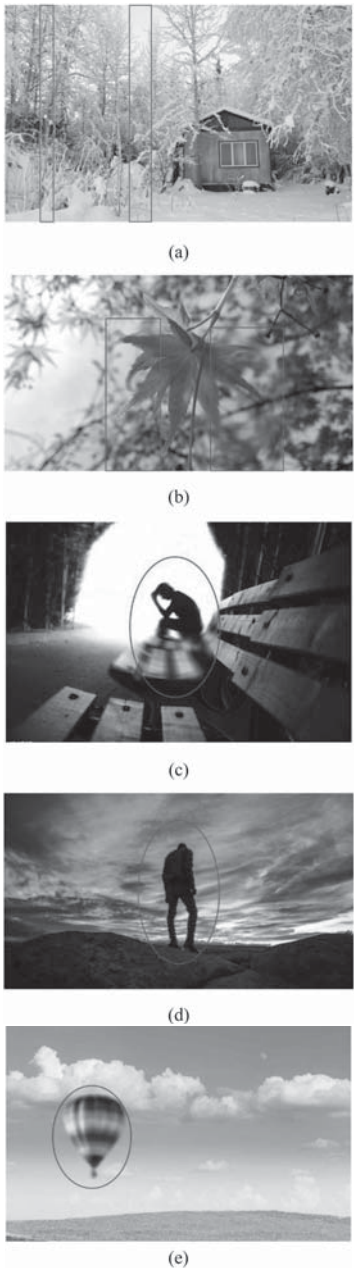

Figure 7 Analysis results of longitudinal deformation of high-resolution integrated image.

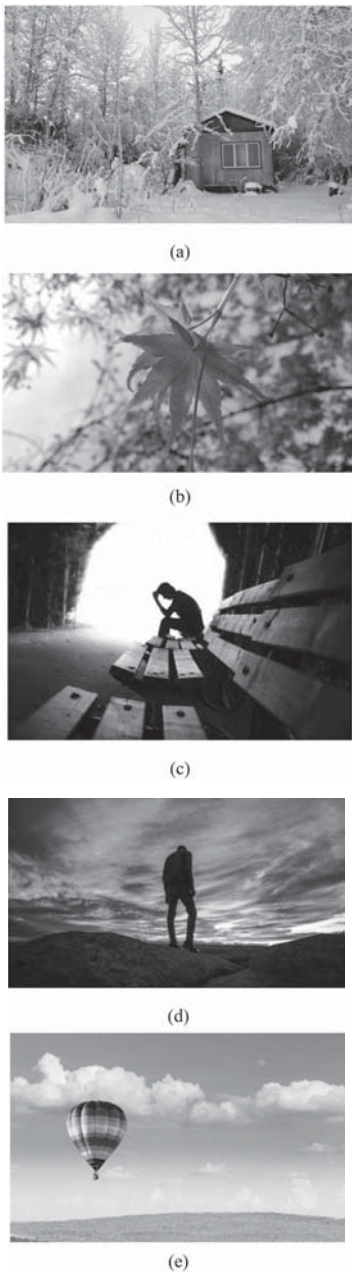

Figure 8 Processing results of longitudinal deformation of high-resolution integrated image.

Table 1 Time of longitudinal deformation analysis of high-resolution integrated image.

Group	Analysis time/s
Group 1	2.56
Group 2	1.45
Group 3	1.36
Group 4	1.84
Group 5	1.56
Group 6	2.13
Group 7	2.01
Group 8	1.75
Group 9	1.56
Group 10	1.35
average value	1.76

deformation of high-resolution integrated image is shorter, the efficiency is greater, and the longitudinal deformation analysis results of high-resolution integrated image can be obtained faster.

4. CONCLUSION

With the development of global intelligent devices, sensors, as intelligent visual sensing devices, are developing along the direction of different spectra, higher resolution and higher acquisition tilt frequency. They have been widely used in scientific research, military operations, transportation, public safety, machine vision and other fields. With more intense research on the mechanism and motion law of high-speed transient phenomenon, the sensor system provides a powerful means for its testing, recording and analysis. Therefore, this paper proposes a high-resolution integrated image longitudinal deformation analysis method based on multi-sensors, and details its implementation process. According to experimental results, the high-resolution integrated image longitudinal deformation analysis effect of this method is better. The high-resolution integrated image processed in this paper has greater definition, shorter comprehensive analysis time and better efficiency, which will broaden its application in practice.

REFERENCES

1. Deng Y, Chen Y, Huang J, et al. Visualization of arc energy distribution based on CCD image sensor. *IOP Conference Series Earth and Environmental Science*, 2020, 617(1):012029–012042.
2. Hattori T, Dasai F, Sato H, et al. CCD multi-ion image sensor with four 128 × 128 pixels array. *Sensors*, 2019, 19(7):1582–1593.
3. Wang S, Brolly R, Carpenter DA, et al. 43- and 50-Mp high-performance interline CCD image sensors. *IEEE Transactions on Electron Devices*, 2019, 66(3):1329–1337.
4. Si Y. Parameter estimation of Poisson-gaussian signal-dependent noise from single image of CMOS/CCD image sensor using local binary cyclic jumping. *Sensors*, 2021, 21(24):8330–8341.
5. Jerram P, Stefanov K. CMOS and CCD image sensors for space applications. *High Performance Silicon Imaging* (Second Edition), 2020, 25(1):255–287.
6. Kagawa K, Horio M, Pham AN, et al. A dual-mode 303-megaframes-per-second charge-domain time-compressive computational CMOS Image Sensor. *Sensors*, 2022, 22(5):1–11.
7. Yang HC, Shin SH, Kumar S, et al. A CMOS image sensor-based refractometer without spectrometry. *Sensors*, 2022, 22(3):25–37.
8. Pérez M, Abbate OI, Lipovetzky J, et al. Neutron imaging based on transfer foil activation and COTS CMOS image sensors. *Journal of Instrumentation*, 2022, 17(2):156–169.
9. Freitas LMC, Morgado Dias F. Design improvements on fast, high-order, incremental sigma-delta ADCs for low-noise stacked CMOS image sensors. *Electronics*, 2021, 10(16):1936–1948.

10. Rahman MH, Sejan MAS, Chung WY. Multi-lateration approach for wide range visible light indoor positioning system using mobile CMOS image sensor. *Applied Sciences*, 2021, 11(16):7308–7322.
11. Nascimento M, Li J, Joseph D. Efficient pipelined circuits for histogram-based tone mapping of nonlinear CMOS image sensors. *Journal of Imaging Science and Technology*, 2021, 65(4):1–13.
12. Deng YK, Chen YP, Huang JS, et al. Visualization of arc energy distribution based on CCD image sensor. *IOP Conference Series: Earth and Environmental Science*, 2020, 617(1):012029–012036.
13. Zhao Y, Chen Z, Luo S. Micro-expression recognition based on pixel residual sum and cropped gaussian pyramid. *Frontiers in Neurorobotics*, 2021, 20(15):746985–746998.
14. Jiao JJ, Wang XP, Zhang JP, et al. Salient region growing based on Gaussian pyramid. *IET Image Processing*, 2021, 15(13):3142–3152.
15. Jing JF, Ren HH. Defect detection of printed fabric based on RGBAAM and image pyramid. *Autex Research Journal*, 2021, 21(2):135–141.
16. Xiao XL, Ren Y, Fang YE. Building settlement monitoring based on multi? Sensor and RBF neural network. *Electronic Design Engineering*, 2021, 29(13):51–55.
17. Zhang C, Wu XP, Lu JC, et al. RICA-MD: A refined ICA algorithm for motion detection. *ACM Transactions on Multimedia Computing Communications and Applications*, 2021, 17(1):1–17.